

A quasiparticle-injection superconducting microwave relaxation oscillator

Giacomo Trupiano,^{*} Giorgio De Simoni,[†] and Francesco Giazotto[‡]

NEST, Istituto Nanoscienze-CNR and Scuola Normale Superiore, Piazza S. Silvestro 3, I-56127 Pisa, Italy

We propose a superconducting microwave relaxation oscillator based on a nanowire shunted by a resistor and an inductor controlled by quasiparticle injection from a tunnel junction positioned on it: the QUISTRON. This device exhibits relaxation oscillator behavior with DC voltage-controlled frequency tuning and DC current bias. The device frequency is modulated via the tunnel junction, which induces localized heating by injecting quasiparticles. This heating mechanism modulates the nanowire switching current, enabling relaxation oscillations when it falls below the bias current. We demonstrate the device operating principles and characterize its performance across various parameters, including different choices of shunt resistor, shunt inductance, and bath temperature ranging from 20 mK to 1 K. The device showed oscillation with a frequency range approximately between 1 GHz and 10 GHz and total energy dissipation per cycle of ~ 100 zJ. Our results suggest that this design offers a promising platform for compact, tunable superconducting oscillators in the microwave spectrum with potential applications in quantum information processing, microwave technology, and ultra-low-power electronics. The straightforward frequency control mechanism and integration potential make this device an attractive candidate for superconducting microwave local oscillators.

I. INTRODUCTION

Superconducting electronics has emerged as a promising platform for quantum information processing [1, 2], ultra-low-power computing [3–5], and high-sensitivity detectors [6–10]. Within this field, superconducting oscillators play a crucial role in various applications, including local control of superconducting qubits [11–14] and clock generators for superconducting digital circuits [15, 16].

Traditionally, Josephson-junction-based oscillators have been the primary choice for superconducting oscillator applications [17, 18]. These devices offer notable advantages, including low power consumption and compatibility with superconducting circuits. However, they often face significant challenges in terms of power output, necessitating large junction arrays. Although practical, this approach introduces scalability issues [18, 19].

Recent advancements in superconducting nanowire technology have opened new avenues for device design. Superconducting nanowires have demonstrated remarkable properties, including high [20–23] and tunable [24, 25] kinetic inductance, strong non-linearity [26, 27], and sensitivity to local thermal perturbations [28, 29]. These characteristics make them attractive candidates for novel oscillator designs.

Using thermal effects to control superconducting devices has gained traction in recent years [30, 31]. Notably, the development of superconducting bolometers [32–35], hot-electron detectors [36], superconducting nanowire single-photon detectors [7, 37–39], superconducting logic [40–44], and

neuromorphic [45–47] circuits based on controlled heating of superconducting nanowires have demonstrated the potential of thermally actuated superconducting devices. On this background, superconducting relaxation oscillators were demonstrated [48, 49], exploiting a design incorporating a superconducting nanowire shunted by a resistor and biased above its switching current.

Here, we propose a superconducting microwave relaxation oscillator based on a nanowire shunted by a resistor and an inductor, which we call QUISTRON. Its operation leverages the thermal sensitivity of the superconducting nanowires and the controllable heat injection through a normal metal-insulator-superconductor (NIS) tunnel junction [50–52] overlapped with the nanowire. Our approach allows for a compact design without needing large arrays of Josephson junctions [18, 19] and, differently from previous nanowire-based oscillators, it takes advantage of the quasiparticle injection and of the localized heating to modulate the nanowire switching current. A voltage-controlled quasiparticle injection scheme allows us to achieve a large-bandwidth tuning range without complex flux-based control schemes.

Furthermore, the simple DC control and the compatibility with standard superconducting fabrication processes may facilitate an easy integration with other superconducting circuit elements. Finally, by leveraging the ultra-low dissipation of superconducting nanowires, the QUISTRON promises an energy efficiency comparable to or better than state-of-the-art superconducting oscillators [17, 18] and to address several challenges in the field of quantum information processing and of superconducting electronics. Indeed, it could serve as a local oscillator for superconducting qubits [11–14], or as a clock generator for superconducting digital circuits [15, 16]. Its tunability could be advantageous in superconducting parametric amplifiers [53]. Moreover, the device

^{*} Corresponding author: giacomo.trupiano@sns.it

[†] Corresponding author: giorgio.desimoni@nano.cnr.it

[‡] Corresponding author: francesco.giazotto@sns.it

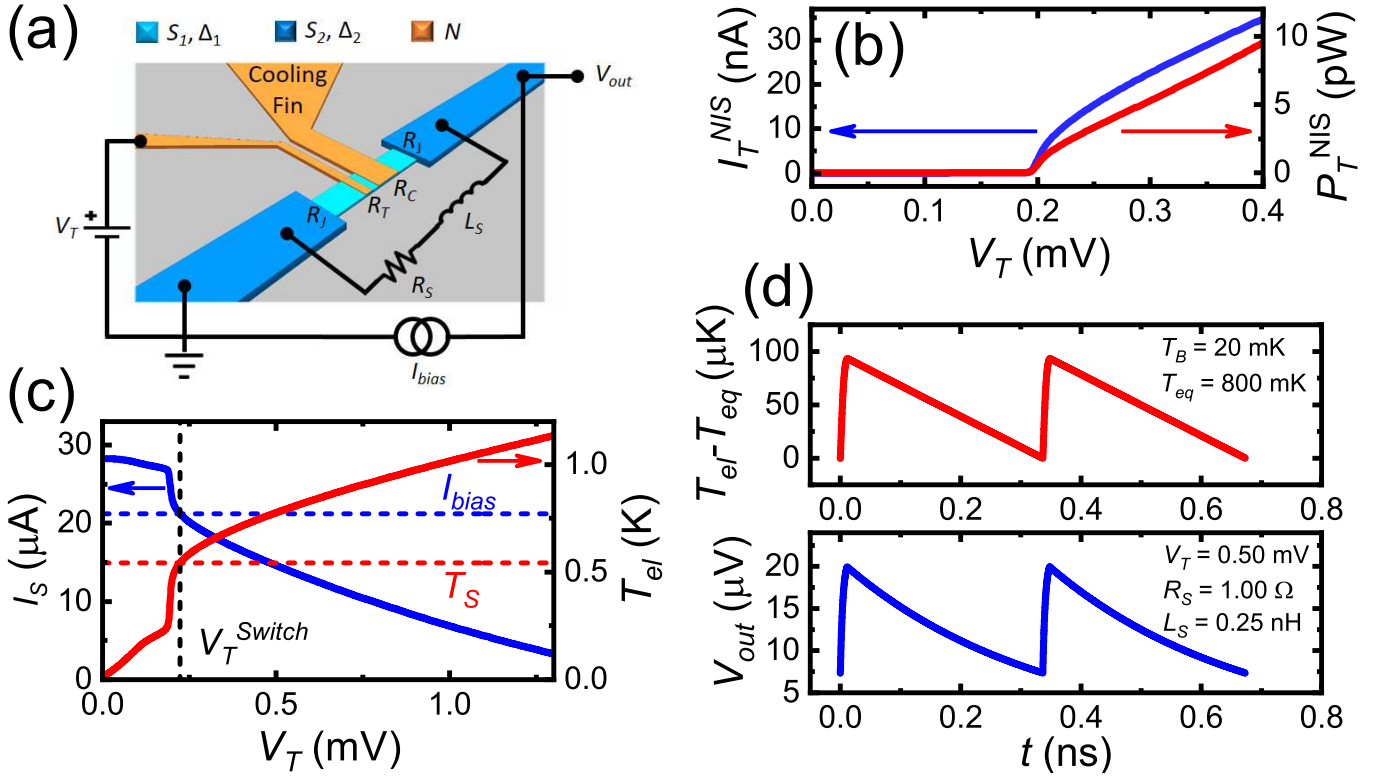


FIG. 1. QUISTRON scheme and operation. (a) Circuit scheme: A superconducting nanowire (S_1 , gap Δ_1 , *e.g.* aluminum) is shunted by a resistor R_S and an inductor L_S , connected to superconducting banks (S_2 , $\Delta_2 > \Delta_1$, *e.g.* niobium) via tunnel junctions with resistance R_J . Additional tunnel junctions with resistances R_T and R_C are placed on the nanowire for quasiparticle injection and cooling, respectively, connected to a normal metal (N) contact and a cooling fin. The injection tunnel junction (R_T) heats the nanowire to enable relaxation oscillations. In contrast, the junction connected to the cooling fin (R_C) dissipates heat generated by Joule heating once the nanowire enters the normal state. (b) Normal metal-Insulator-Superconductor (NIS) junction characteristics: Charge (I_T , blue, left y -axis) and heat (P_T , red, right y -axis) currents vs. V_T at bath temperature $T_B = 20$ mK. The NIS junction is insulating for subgap voltages; current increases rapidly at $V_T \simeq \Delta_1/e = 0.2$ mV. (c) Nanowire switching current (I_S , continuous blue line, left y -axis) and electronic temperature (T_{el} , continuous red line, right y -axis) vs. V_T . I_S drops sharply at $V_T \simeq \Delta_1/e$ due to increased heat current and electronic temperature. The blue dashed line indicates the I_{bias} value used in simulations shown in Fig. 4 and Fig. 5, and the black dashed line indicates switching voltage V_T^{Switch} , which is the voltage needed to have $I_S = I_{bias}$. The red dashed line indicates the switching electronic temperature T_S . (d) Simulated T_{el} and voltage oscillations at $V_T = 0.50$ mV, $T_B = 20$ mK, $R_S = 1 \Omega$, $L_S = 0.25$ nH. T_{el} spikes and cooling correspond to the nanowire switching between normal and superconducting states. Voltage oscillations result from the current redistribution between the nanowire and the shunt when the nanowire changes its state. The inverse of the oscillation period is $\nu_0 = 3$ GHz.

capability to generate multiple harmonics envisages its employment as a frequency source for multiplexed readout systems. This feature is precious for transition edge sensors (TES) [6, 54] and kinetic inductance devices (KID) [8, 9, 55], both of which play crucial roles in many astrophysics applications [34, 35, 56].

In the following sections, we present the device concept, the theoretical framework, and the results of numerical simulations. We investigate device performance across various parameters, including shunt resistance, inductance values, and operating temperature. Finally, we discuss the potential applications and prospects of the QUISTRON in the context of quantum information processing, microwave technology, and ultra-low-power electronics.

II. OPERATION OF THE DEVICE

Fig. 1(a) shows the core of the QUISTRON: a superconducting nanowire (S_1) with a superconducting gap Δ_1 , shunted by a resistor R_S and an inductor L_S . The nanowire connects to superconducting banks (S_2) with a larger superconducting gap ($\Delta_2 > \Delta_1$) via tunnel junctions (resistance R_J). The key in our design is the addition of two specialized tunnel junctions on the nanowire. The first, with resistance R_T , connects to a normal metal (N) electrode and is the quasiparticle injection point for heating the nanowire. The second, with resistance R_C , connects to a cooling fin to dissipate heat generated when the nanowire transitions to the normal state. In this work, we assume the nanowire to

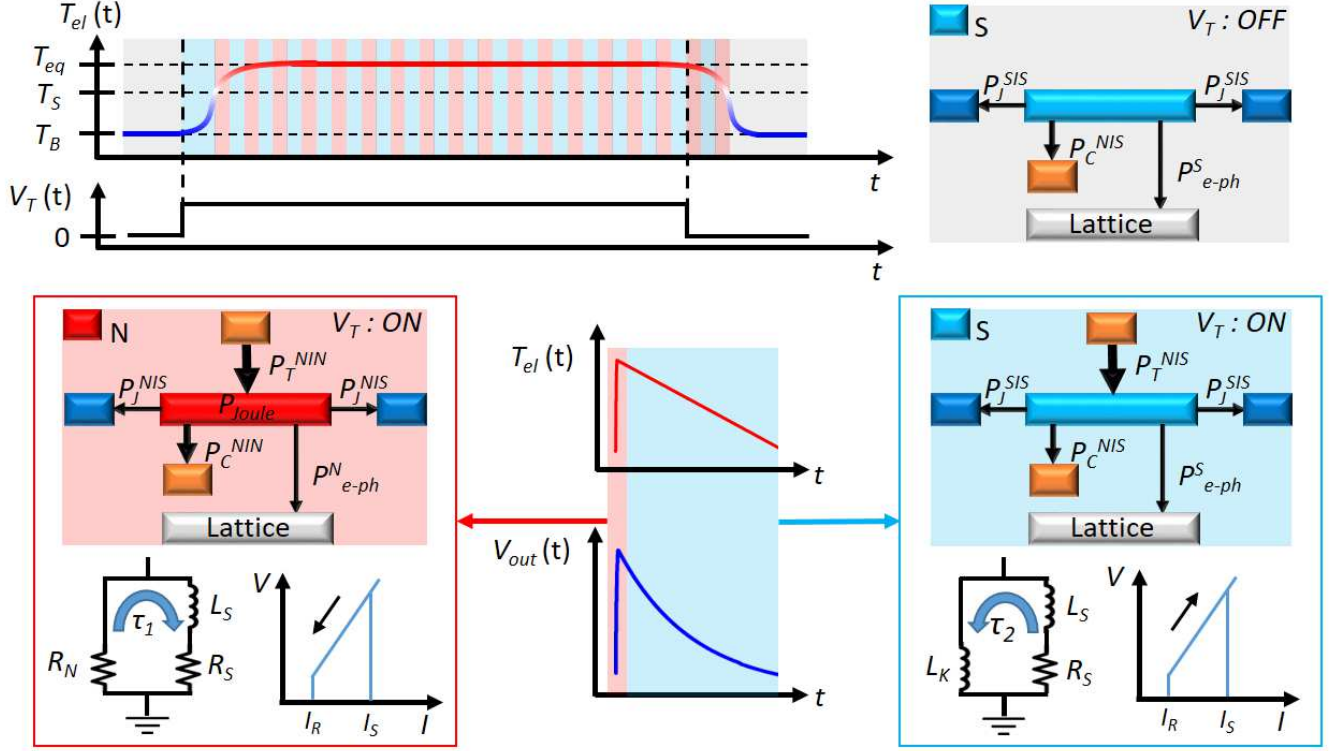


FIG. 2. Schematic of the QUISTRON operating principle, heat currents, and voltage and temperature oscillations. The color code indicates nanowire states and heat currents: blue (superconducting, voltage ON), red (normal, voltage ON), and grey (superconducting, voltage OFF). Oscillations are controlled by a tunnel junction voltage (V_T) applied to the nanowire. When $V_T = 0$, the nanowire electronic temperature (T_{el}) is at equilibrium with the bath temperature (T_B), maintaining superconductivity. As V_T exceeds Δ_1/e (Δ_1 : superconducting gap), T_{el} increases due to quasiparticle injection (blue to red color gradient in the upper-left scheme). When V_T surpasses a critical value V_T^{Switch} , T_{el} exceeds the switching temperature T_S , transitioning the nanowire to its normal state. The bias current redirects to the shunt resistor R_S with characteristic time $\tau_1 = L_S/(R_S + R_N)$, where L_S is the shunt inductance, R_S the shunt resistance, and $R_N = R_{NW} + 2R_J$ is the total normal state resistance of the series of the two Josephson junctions R_J and the nanowire. This generates V_{out} and further heats the nanowire. As the nanowire current falls below the retrapping current I_R , it reverts to the superconducting state. Current then redirects back to the nanowire with characteristic time $\tau_2 = (L_S + L_K)/R_S$, where L_K is the kinetic inductance. Consequently, V_{out} decreases. T_{el} rises during oscillations until reaching equilibrium temperature T_{eq} , where heating during the normal state balances cooling while in the superconducting state. This process repeats cyclically, producing periodic oscillations in V_{out} and T_{el} until V_T is set to zero. The nanowire oscillates while T_{el} gradually decreases. When T_{el} falls below T_S , oscillations cease, and T_{el} returns to the bath temperature T_B (red to blue color gradient in the upper-left scheme).

be made of aluminum, with a gap $\Delta_1 = 0.2$ meV and a critical temperature $T_{c1} = 1.3$ K, and the banks to be made of niobium, with a gap $\Delta_2 = 1.4$ meV and a critical temperature $T_{c2} = 9.2$ K. The operation of the device relies on the controlled injection of quasiparticles through the tunnel junction to regulate the electronic temperature of the nanowire. Fig. 1(b) illustrates the NIS (Normal metal-Insulator-Superconductor) junction characteristics, showing charge (I_T^{NIS}) and heat (P_T^{NIS}) currents versus applied voltage V_T at a bath temperature of 20 mK. The NIS junction is insulating for subgap voltages, with currents increasing steeply at $V_T \simeq \Delta_1/e = 0.2$ mV, where e is the elementary charge. The S_2 banks play a crucial role in enhancing the device efficiency by confining the injected quasiparticles within the nanowire. This confinement occurs because $\Delta_2 >$

Δ_1 , causing the S_2IS_1 junctions to act as Andreev mirrors for the quasiparticles [30, 57]. Fig. 1(c) shows how the nanowire switching current (I_S) and electronic temperature (T_{el}) vary with V_T . I_S drops sharply at $V_T \simeq \Delta_1/e$ due to increased heat current and T_{el} . This graph also indicates the bias current (I_{bias}) used in our simulations and the switching voltage (V_T^{Switch}), which is the voltage needed to have $I_S = I_{bias}$. Fig. 1(d) shows the voltage and temperature oscillations, which are controlled by the tunnel junction voltage (V_T). When V_T exceeds a critical value, the nanowire electronic temperature (T_{el}) rises above the switching temperature (T_S), causing a transition to the normal state. This redirects the bias current to the shunt resistor, generating V_{out} and further heating the nanowire. As the nanowire current drops below the retrapping current I_R , it returns

to the superconducting state, redirecting current back to the nanowire. This cycle repeats, creating periodic oscillations in V_{out} and T_{el} until V_T is set to zero. The process involves characteristic times τ_1 and τ_2 , which depend on various circuit parameters. This mechanism is explained in detail in the next paragraph and illustrated in Fig. 2.

The oscillation microscopic mechanism is illustrated in Fig. 2. When $V_T = 0$, the nanowire electronic temperature (T_{el}) is at equilibrium with the bath temperature (T_B), maintaining superconductivity (Fig. 2, grey regions). As V_T exceeds Δ_1/e , T_{el} increases due to quasiparticle injection (Fig. 2, blue regions). When V_T surpasses the critical value V_T^{Switch} , T_{el} exceeds the switching temperature T_S , transitioning the nanowire to its normal state. This causes the bias current to redirect toward the shunt resistor R_S with a characteristic time $\tau_1 = L_S/(R_S + R_N)$, where L_S is the shunt inductance and $R_N = R_{NW} + 2R_J$ is the total normal-state resistance of the series of the two Josephson junctions R_J and the nanowire. This generates the output voltage V_{out} and further heats the nanowire (Fig. 2, red regions). As the nanowire current falls below the retrapping current I_R , it reverts to the superconducting state. The current then redirects back to the nanowire with characteristic time $\tau_2 = (L_S + L_K)/R_S$, where L_K is the total kinetic inductance of the series of the two Josephson junctions R_J and the nanowire, causing V_{out} to decrease (Fig. 2, blue regions). This process repeats cyclically, producing periodic oscillations in V_{out} and T_{el} , as shown in Fig. 1(d). The simulation shown in Fig. 1(d) was performed at $V_T = 0.50$ mV, $T_B = 20$ mK, $R_S = 1$ Ω , and $L_S = 0.25$ nH, and it shows T_{el} spikes corresponding to the nanowire switching between normal and superconducting states. The resulting voltage oscillations have a $\nu_0 = 3$ GHz frequency. The temperature and voltage oscillations continue until V_T is set to zero (Fig. 2, grey region), causing T_{el} to decrease gradually. When T_{el} falls below T_S , oscillations cease, and T_{el} returns to T_B .

The heat transport mechanisms are represented in schemes within colored regions. The blue area depicts the heat currents scheme when the nanowire is superconducting and the tunnel junction is injecting, where $P_T^{NIS}(T_{el}, V_T)$ is the heat current of the injection junction, $P_C^{NIS}(T_{el})$ is the heat current flowing through the cooling fin, $P_J^{SIS}(T_{el})$ is the heat current through the leads, and $P_{e-ph}^S(T_{el})$ is the electron-phonon coupling heat current. The red region shows the heat currents scheme when the nanowire is in the normal state and the tunnel junction is injecting, where $P_T^{NIN}(T_{el}, V_T)$ is the heat current of the injection junction, P_{Joule} is the Joule heating power, $P_C^{NIN}(T_{el})$ is the heat current flowing through the cooling fin, $P_J^{SINIS}(T_{el}, V_{out})$ is the heat current through the series of the two junctions and the nanowire, and $P_{e-ph}^N(T_{el})$ is the electron-phonon coupling heat current. The grey region illustrates the heat currents scheme when the nanowire is superconducting,

and the tunnel junction is not injecting. These heat currents were used to simulate the thermal dynamics of the device, as described in the following section. The detailed calculations of these heat currents are provided in Appendix A.

The characteristic times τ_1 and τ_2 represent the timescales for current redistribution between the nanowire and shunt resistor, influencing the shape and frequency of the oscillations. The oscillation frequency depends on the characteristic L/R time of the circuit and I_{bias} , I_S , and I_R . An approximated relation for the period of a single relaxation oscillation is [48, 49]:

$$T = \frac{1}{\nu_0} \simeq \tau_1 \log\left(\frac{I_S}{I_R}\right) + \tau_2 \log\left(\frac{I_{bias} - I_R}{I_{bias} - I_S}\right), \quad (1)$$

where all quantities dependent on the electronic temperature T_{el} , such as τ_2 (through L_K) and I_S , are evaluated at the equilibrium temperature T_{eq} . For this reason, it is possible to modulate the frequency by changing the voltage applied to the injection junction, V_T . By increasing V_T , we can increase the power injected and, thus, the electronic temperature of the nanowire. Since I_S monotonically decreases with increasing T_{el} , while I_{bias} remains constant, the oscillation frequency increases accordingly.

A similar mechanism was previously exploited to realize a superconducting relaxation oscillator based on a shunted superconducting nanowire [48, 49] current biased above its switching current. In this implementation, the oscillation frequency was modulated by increasing or decreasing the bias current with respect to the switching current. The main difference in our approach is that we can control the oscillation by applying a voltage to the injection junction while keeping I_{bias} constant. This allows us to control the relaxation oscillation using a much smaller current. Indeed, as shown in Fig. 1(c), it is sufficient to apply $V_T \simeq 0.25$ mV, which corresponds to the injection of a tunnel current $I_T \lesssim 20$ nA, as shown in Fig. 1(b). If we used the bias current to control the oscillation frequency, we would have to change it by a sizable portion of the switching current, around 10 μ A.

III. CIRCUIT MODEL AND RELAXATION OSCILLATIONS SIMULATION

A. Circuit Design and Parameter Choices

The circuit parameters used in the calculations were: $R_T = 10$ k Ω , $R_C = 500$ Ω , and $R_J = 10$ Ω , while we simulated the device for different choices of R_S and L_S , as shown in Fig. 4 and Fig. 5. The choices of R_T and R_C allowed to achieve good electronic input-output insulation between the nanowire and the injection junction ($R_T \gg R_N$), efficient heating while the nanowire is superconducting ($P_T^{NIS} \gg P_C^{NIS}$), and effective heat dispersion through the cooling fin when the nanowire is in the normal state ($P_C^{NIN} \sim P_T^{NIN}$, P_{Joule}).

The cooling fin provides an innovative and simple method for introducing passive feedback control on the electronic temperature of the nanowire. This is because the heat current flowing through the junction connected to the cooling fin is heavily dependent on the state of the nanowire. Given that the gapped density of states in the superconductor suppresses quasiparticle tunneling, we have $P_C^{NIS} \ll P_C^{NIN}$. Consequently, the heat current dispersed through the cooling fin is negligible when the nanowire is superconducting, enhancing the heating process efficiency. Conversely, when the nanowire is in the normal state, the heat current dispersed through the cooling fin is comparable to the Joule heating, thus preventing runaway heating of the nanowire.

The nanowire switching current dependence was estimated using the Bardeen equation for a dirty superconductor [58]:

$$I_S(T_{el}) = \frac{J_c(0)wt}{2\sqrt{2}} \left[1 - \left(\frac{T_{el}}{T_{c1}} \right)^2 \right]^{3/2}, \quad (2)$$

where $J_c(0) = 100 \text{ GA/m}^2$ is the nanowire critical current density at 0 K, $w = 40 \text{ nm}$ is its width, and $t = 20 \text{ nm}$ is its thickness. The critical current density value is extracted by [59], where the J_c of aluminum films of different thicknesses is analyzed down to $t = 20 \text{ nm}$. With this choice of parameters, the maximum switching current of the aluminum nanowire is estimated to be $I_S^{max} \simeq 28 \text{ } \mu\text{A}$. The film resistivity is also provided in the same work [59]. In particular, the resistivity of a 20-nm-thick film is $\rho_{Al} \simeq 26 \text{ n}\Omega\text{m}$. Using this result, we can extrapolate the normal-state resistance of the nanowire to be $R_{NW} = \rho_{Al}(l/wt) \simeq 40 \text{ } \Omega$, where $l = 1.2 \text{ } \mu\text{m}$ is the length of the nanowire used in our calculation. Thus, the total normal-state resistance of the series combination of the two Josephson junctions R_J and the nanowire is $R_N = R_{NW} + 2R_J \simeq 60 \text{ } \Omega$. The R_J resistance was chosen to be equal to $10 \text{ } \Omega$ so that the critical current of the Josephson junction formed by the S_2IS_1 junctions (I_c) would be larger than the switching current of the nanowire. This requirement simplifies the dynamics, as we can treat the two Josephson junctions as (Andreev) mirrors for quasiparticles.

The Josephson junction critical current (I_c) and its temperature dependence were calculated using the Ambegaokar-Baratoff relation [60, 61]:

$$I_c(T_{el}) = \frac{\pi\Delta_1(T_{el})}{2eR_J} \tanh \left[\frac{\Delta_1(T_{el})}{2k_B T_{el}} \right], \quad (3)$$

where k_B is the Boltzmann constant, and the gap dependence on the electronic temperature was estimated using the numerical approximation of the gap equation solution [62]:

$$\Delta_1(T_{el}) \simeq \Delta_1 \tanh \left(1.74 \sqrt{\frac{T_{c1}}{T_{el}}} - 1 \right). \quad (4)$$

With this choice of parameters, the maximum critical current of the Josephson junctions was estimated to be $I_c^{max} \simeq 31 \text{ } \mu\text{A}$. It is important to note that the condition $I_c^{max} > I_S^{max}$ is not strictly necessary to ensure the correct operation of the device. This is because the nanowire switching current dependence on the electronic temperature is steeper than that of the Josephson critical current. It is sufficient that the bias current intersects the $I_S(T_{el})$ curve before the $I_c(T_{el})$ curve. This condition ensures that the nanowire switches to the normal state before the Josephson junctions lose their superconductivity so that the dynamics of the device is controlled only by the state of the nanowire. This relaxed condition provides more flexibility in the design and operation of the device, allowing for a broader range of parameters while still maintaining the core functionality of the QUISTRON.

The Josephson junctions were designed to be non-hysteretic to ensure their critical current and switching current were larger than the nanowire switching current. We used high-transparency Josephson junctions to achieve this, as shown in [63]. We assumed typical values for the specific capacitance $c_s = 50 \text{ fF}/\mu\text{m}^2$ and a low but experimentally feasible specific resistance $r_s = 20 \text{ } \Omega/\mu\text{m}^2$ [63]. With these parameters, we estimated a Stewart-McCumber parameter $\beta_c \simeq 0.9$, indicating the non-hysteretic behavior of the Josephson junction [61].

One possible design for the QUISTRON involves directly connecting the aluminum superconducting nanowire to the niobium banks without an insulating interface. Without the insulating interface, the larger superconducting gap of the banks would still serve as Andreev mirrors for the quasiparticles in the nanowire, effectively trapping the heat in the nanowire. However, we opted to include insulating interfaces with resistance R_J in the device design. This approach simplified the modeling of the heat current between the nanowire and the banks by providing a well-defined interface and ensuring better thermal insulation. Additionally, it avoids the complications introduced by the proximity effect between the two superconductors [64]. Nonetheless, this alternative design could be easier to implement and should be considered in future research.

B. Steady-state simulations

Steady-state simulations were performed to understand the behavior of QUISTRON. These simulations aimed to identify two main parameters: the steady-state electronic temperature achieved by the superconducting nanowire when starting from its equilibrium state with the bath temperature, and the switching current based on the applied injection voltage. The initial simulations focused on characterizing the heat current of the injection junction in relation to the injection voltage while the nanowire remained superconducting. Heat transfer calculations supported

these simulations through three pathways: the leads, the cooling fin, and the electron-phonon coupling mechanism. The overall heat balance was determined by adding the contributions from these pathways with their respective signs: heat current flowing into the nanowire was considered positive, while heat current flowing out of the nanowire was considered negative. To find the steady-state electronic temperature of the nanowire, T_{el} , as a function of V_T , we solved the heat balance equation for T_{el} :

$$P_T^{NIS}(V_T, T_{el}) - P_J^{SIS}(T_{el}) - P_C^{NIS}(T_{el}) - P_{e-ph}^S(T_{el}) = 0, \quad (5)$$

where $P_T^{NIS}(V_T, T_{el})$ is the heat current of the injection junction when the nanowire is superconducting, shown in Fig. 1(b), $P_J^{SIS}(T_{el})$ is the heat current flowing through the leads, $P_C^{NIS}(T_{el})$ is the heat current flowing through the cooling fin, and $P_{e-ph}^S(T_{el})$ is the heat current due to the electron-phonon coupling (see Appendix A for details). By solving this equation, we obtained the steady-state electronic temperature as a function of the applied injection voltage, $T_{el}(V_T)$, which is represented by the red curve in Fig. 1(c). Using this relationship and the Bardeen relation between the switching current and the electronic temperature, $I_S(T_{el})$, as shown in Eq. (2), we can estimate the dependence of the switching current on the applied voltage, $I_S(V_T)$, represented by the blue curve in Fig. 1(c).

Once the $I_S(V_T)$ relation is known, we can estimate the voltage needed to switch the nanowire to the normal state for a given bias current I_{bias} . This is the voltage V_T^{Switch} needed to lower I_S to the value of I_{bias} . In this simulation, we chose a bias current that is 75% of the switching current evaluated at the bath temperature ($T_B = 20$ mK). For this value of I_{bias} , we estimate $V_T^{Switch} = 0.22$ mV, which corresponds to a switching temperature $T_S = 0.54$ K, as it is shown in Fig. 1(c).

C. Dynamics simulation

The relaxation oscillation dynamics was simulated by solving the heat equation of the nanowire. This took into account various heat currents and electronic heat capacity, both when the nanowire is superconducting and in the normal state (see Fig. 2 for red regions and heat currents scheme). The simulation starts when the nanowire reaches the switching temperature T_S , causing it to transition to the normal state. In this state, the dynamics of the electronic temperature of the nanowire is described by the differential equation

$$C_N \frac{dT_{el}}{dt} = P_T^{NIS}(T_{el}, V_T) + P_{Joule} - P_C^{NIS}(T_{el}) - P_J^{SIS}(T_{el}, V_{out}) - P_{e-ph}^N(T_{el}), \quad (6)$$

with the initial condition for the temperature being $T_{el}(0) = T_S$, where C_N is the nanowire electronic heat

capacity in the normal state (see Appendix B for details on its estimation), $P_T^{NIS}(T_{el}, V_T)$ is the heat current of the injection junction, P_{Joule} is the Joule heating power, $P_C^{NIS}(T_{el})$ is the heat current flowing through the cooling fin, $P_J^{SIS}(T_{el}, V_{out})$ is the heat current through the series of the two junctions and the nanowire, and $P_{e-ph}^N(T_{el})$ is the electron-phonon coupling heat current (see Appendix A for details on their estimations and red shaded areas in Fig. 2 for schematic representation of the heat currents). In this equation, we neglect the spatial gradient of the temperature because, at the operation temperature ($T < T_{c1}$), the nanowire dimensions are smaller than the electron-phonon scattering length (see Appendix B for details on its estimation). This condition ensures that the dynamics of the heat currents are approximately homogeneous along the entire nanowire.

To consistently calculate $P_J^{SIS}(T_{el}, V_{out})$, and especially the heat due to the Joule effect $P_{Joule} = V_{out}(t)I_{NW}(t)$, we have to estimate the time dependence of $V_{out}(t)$ and $I_{NW}(t)$, which are the voltage applied across the nanowire and the charge current flowing through it. We know that the initial condition for the current flowing through the nanowire is $I_{NW}(0) = I_S(T(0) = T_S)$ because the nanowire switches to the normal state at $t = 0$. We assume that the transition to the normal state is instantaneous ($\hbar/\Delta_1 \sim 10$ ps, much smaller than other characteristic times τ_1 and τ_2) so that the circuit made by the shunted nanowire instantaneously becomes an RL circuit with time constant $\tau_1 = L_S/(R_N + R_S)$. Thus, the time dependence of the current flowing through the nanowire and of the voltage drop across it are, respectively:

$$I_{NW}(t) = (I_S(T(0)) - I_{min})e^{-\frac{t}{\tau_1}} + I_{min}, \quad (7)$$

$$V_{out}(t) = R_{\parallel}(I_{bias} - I_{NW}(t)), \quad (8)$$

where $I_{min} = I_{bias}R_{\parallel}/R_N$ is the minimum current that can flow through the nanowire when the circuit is at steady state, $R_{\parallel} = (1/R_N + 1/R_S)^{-1}$ is the parallel resistance of the shunted nanowire, and τ_1 is the RL characteristic time of the circuit.

While the nanowire is normal, its electronic temperature rises, primarily due to heating from the Joule effect. The simulation ends when the current flowing through the nanowire equals its retrapping current (I_R): $I_{NW}(t_{final}) = I_R$ (see Appendix C for details on the estimation of the retrapping current). When this occurs, the nanowire instantaneously transitions to the superconducting state, thereby changing the dynamics of the heat and charge currents (Fig. 2 blue regions and heat currents scheme). In this state, the dynamics of the electronic temperature of the nanowire is described by the differential equation:

$$C_S \frac{dT_{el}}{dt} = P_T^{NIS}(T_{el}, V_T) - P_C^{NIS}(T_{el}) - 2P_J^{SIS}(T_{el}) - P_{e-ph}^S(T_{el}), \quad (9)$$

with the initial condition for the temperature being $T_{el}(0) = T_{final}$, where T_{final} is the temperature reached

at the end of the simulation described by Eq. (6). Here, C_S is the nanowire electronic heat capacity in the superconducting state (see Appendix B for details on its estimation), $P_T^{NIS}(T_{el}, V_T)$ is the heat current of the injection junction, $P_C^{NIS}(T_{el})$ is the heat current flowing through the cooling fin, $P_J^{SIS}(T_{el})$ is the heat current through the leads, and $P_{e-ph}^S(T_{el})$ is the electron-phonon coupling heat current (see Appendix A for details on their estimations and blue shaded areas in Fig. 2 for schematic representation of the heat currents).

Also, in this case, the simulation of the thermal dynamics is bound to the dynamics of the current flowing through the nanowire. That is because the simulation described in Eq. (9) ends when $I_{NW} = I_S$, causing the switching of the nanowire to the normal state. We know that the initial condition for the current flowing through the nanowire is $I_{NW}(0) = I_R$ because the nanowire switches to the superconducting state at $t = 0$. We assume, again, that the transition is instantaneous so that the circuit instantaneously becomes an RL circuit with time constant $\tau_2(T_{el}) = [L_S + L_K(T_{el})]/R_S$, where L_K is the kinetic inductance of the series of the two junctions and the nanowire (see Appendix C for details on its estimation). Thus, the time dependence of the current flowing through the nanowire and the voltage drop across it are, respectively:

$$I_{NW}(t) = (I_{bias} - I_R) \left(1 - e^{-\frac{t}{\tau_2(T_{el}(t))}} \right) + I_R, \quad (10)$$

$$V_{out}(t) = R_S(I_{bias} - I_{NW}(t)), \quad (11)$$

where we approximated $\tau_2(T_{el}(t)) \simeq \tau_2(T_{el}(0))$, since the thermal oscillations ($\sim 100 \mu\text{K}$) are much smaller than the absolute temperature of operation ($\sim 100 \text{mK}$).

While the nanowire is superconducting, there are two possible dynamics for the electronic temperature. If the electronic temperature is lower than the steady-state temperature $T_{el}(V_T)$ (shown in Fig. 1(c), red curve), the temperature continues to rise. Conversely, if the electronic temperature exceeds this value, the electronic temperature of the nanowire decreases while it is superconducting. However, even in the latter case, this cooling mechanism does not immediately balance the heating stemming from the Joule effect while in the normal state. Consequently, the final temperature reached exceeds the initial switching temperature T_S .

As the simulations described in Eq. (6) and Eq. (9) are cyclically repeated, the final temperature reached at the end of each cycle increases until the cooling mechanisms balance the heating ones (see Fig. 2, blue to red color gradient in the upper-left scheme). This temperature is defined as the equilibrium temperature T_{eq} of the device (see Fig. 2 upper-left scheme). At this temperature, T_{el} and V_{out} periodically oscillate at a defined frequency ν_0 , which depends on the equilibrium temperature, through the switching current dependence on the temperature and the period dependence on it, shown in Eq. (1), and ultimately on the injection voltage V_T . The oscillation frequency can thus be modulated by

applying a DC voltage to the injection tunnel junction. It is noteworthy that under these operating conditions, the bias current consistently exceeds the switching current at the equilibrium temperature, as $T_{eq} > T_S$, implying $I_S(T_{eq}) < I_S(T_S) = I_{bias}$. This oscillation mechanism bears similarities to those reported by [48, 49]. However, our approach offers the advantage of simple frequency modulation by applying a small voltage to the injection junction.

IV. ANALYSIS OF PERFORMANCE

A. Harmonic content and frequency modulation

To analyze the spectral characteristics of the QUISTRON, we performed a frequency analysis of the voltage oscillations for various injection junction voltages (V_T). Figure 3 presents the frequency spectrum of voltage oscillations between 0 and 30 GHz, with fixed $R_S = 1.00 \Omega$, $L_S = 0.25 \text{ nH}$, and bath temperature $T_B = 0.02 \text{ K}$. Figure 3 illustrates the spectrum of the output voltage V_{out} for three different tunnel junction voltages, demonstrating the device voltage-controlled frequency tuning capability. In Fig. 3(a), with $V_T = 1.00 \text{ mV}$, we observe the highest fundamental frequency of $\nu_0 = 8.7 \text{ GHz}$ among the three cases. This corresponds to the fastest oscillations due to the higher applied voltage. As we reduce V_T to 0.50 mV in Fig. 3(b), the fundamental frequency decreases to $\nu_0 = 3.0 \text{ GHz}$. This substantial change in oscillation frequency shows the sensitivity of our device to the applied tunnel junction voltage. Further reducing V_T to 0.25 mV , as shown in Fig. 3(c), results in the lowest fundamental frequency among the three cases: $\nu_0 = 1.2 \text{ GHz}$. This trend clearly illustrates the inverse relationship between the applied voltage and the oscillation period. The spectra reveal not only the fundamental frequencies but also higher harmonics. This harmonic content directly results from the strongly non-sinusoidal oscillation of V_{out} , a typical characteristic of relaxation oscillators.

In addition, we can notice that a DC component is present in each spectrum, as usually observed in this kind of device [48, 49]. This is because, during the oscillation, there is always a current flowing through the shunt resistor that is at least equal to $I_{bias} - I_S$, which generates a voltage $V_{offset} \simeq R_S(I_{bias} - I_S)$. It is possible to remove the offset in V_{out} [45, 46] by using two shunted nanowires in parallel biased in reverse one respect to the other. It is important to note that as the applied voltage increases, the electronic temperature of the nanowire also rises. This has a significant impact on the voltage oscillations. Specifically, it reduces the voltage swing of the oscillations. The increase in temperature leads to a decrease in the switching current relative to the bias current. Consequently, a greater fraction of the current circulates through the shunt resistor, resulting in an increased voltage offset in V_{out} . As the voltage offset

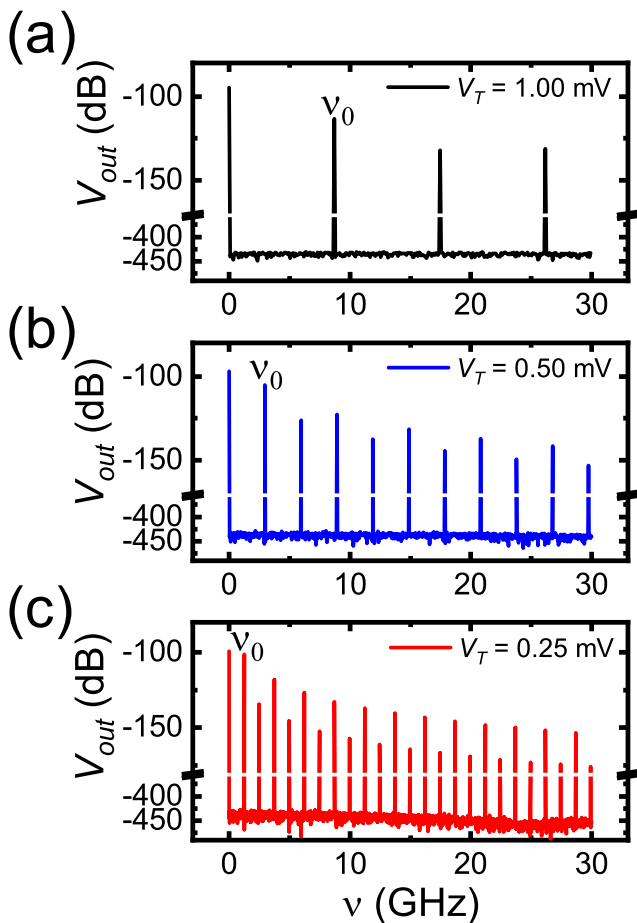


FIG. 3. Frequency spectrum of voltage oscillation vs. V_T between 0 and 30 GHz, for fixed parameters $R_S = 1.00 \Omega$, $L_S = 0.25$ nH, and bath temperature $T_B = 0.02$ K. The spectrum is shown for three different tunnel junction voltages, showing the dependence of oscillation frequency on V_T . (a) Spectrum of output voltage V_{out} for $V_T = 1.00$ mV. The fundamental frequency, the inverse of the oscillation period, is $\nu_0 = 8.7$ GHz. This higher voltage results in the fastest oscillations among the three cases. (b) Spectrum of V_{out} for $V_T = 0.50$ mV. The fundamental frequency is $\nu_0 = 3.0$ GHz, showing a significant decrease in oscillation frequency compared to (a) as V_T is reduced. This is the Fourier transform of the V_{out} signal shown in Fig. 1(d). (c) Spectrum of V_{out} for $V_T = 0.25$ mV. The fundamental frequency is $\nu_0 = 1.2$ GHz, the lowest oscillation frequency of the three cases due to the lowest applied voltage. As V_T increases, the ratio between the first harmonic and the DC component amplitudes decreases. Higher V_T raises the electronic temperature of the nanowire, reducing I_S relative to I_{bias} . Thus, more current flows through the shunt resistor, increasing the voltage offset in V_{out} and decreasing the voltage swing during oscillation. Excessive V_T increases oscillation frequency but reduces amplitude until the device latches.

increases while the maximum of V_{out} remains constant at $R_{||}I_{bias}$ (where $R_{||}$ is the parallel resistance of the shunt and nanowire), the overall swing of voltage during the oscillation decreases. This behavior is illustrated in

Fig. 3, where the ratio between the first harmonic and the zero frequency (DC component) amplitude decreases as a function of V_T . If the injection voltage applied is too large, the oscillation frequency rises, but the oscillation amplitude decreases until the device effectively latches.

Our research demonstrates that the QUISTRON can be adjusted across a broad frequency range, from approximately 1.2 GHz to 8.7 GHz, by modifying the tunnel junction voltage V_T . This adjustable feature, along with the device small size and simple control mechanism, positions it as a highly promising option for various uses in superconducting electronics and quantum information processing. The precise control of the oscillation frequency through a DC voltage provides significant advantages for circuit design and integration. Moreover, the output signal rich harmonic content could be beneficial for applications requiring non-sinusoidal waveforms or frequency multiplication.

B. Impact of shunt resistor and inductor

To understand the influence of circuit parameters on the QUISTRON performance, we investigated the device behavior for different shunt inductance (L_S) and resistance (R_S) values. Figure 4 and 5 present key figures of merit as functions of the tunnel junction voltage V_T , allowing us to analyze the impact of L_S and R_S separately.

Figure 4 shows the device characteristics for selected L_S values, with fixed $R_S = 1.00 \Omega$ and bath temperature $T_B = 0.02$ K. In Fig. 4(a), we observe that the inverse of the oscillation period, ν_0 , increases monotonically with V_T for all L_S values, demonstrating the voltage-controlled nature of the QUISTRON. However, larger L_S values result in lower ν_0 for a given V_T . This behavior can be attributed to the increased characteristic time of the RL circuit formed by the nanowire and the shunt, which slows down the current redistribution process during oscillations. The sensitivity of the oscillator frequency to voltage changes is quantified by the frequency-to-voltage transfer function τ_ν , shown in Fig. 4(b). We obtained τ_ν by calculating the derivative of a cubic spline fit to the data in Fig. 4(a) with respect to V_T . This figure of merit underlines the device oscillation frequency sensitivity to the applied voltage V_T . For every mV applied on the injection junction, the oscillation frequency changes on the 1-10 GHz order. The device oscillation frequency becomes more sensitive to V_T as the L_S decreases because a larger L_S increases the characteristic time of the RL circuit.

Figure 4(c) presents the total energy dissipated per period, E_d , as a function of V_T . We calculated E_d by integrating the sum of all heat currents flowing into the nanowire, Joule power, and energy in every inductor and capacitor over one oscillation period $T = 1/\nu_0$. That can be divided into the integral of the power dissipated when the nanowire is in the normal state and

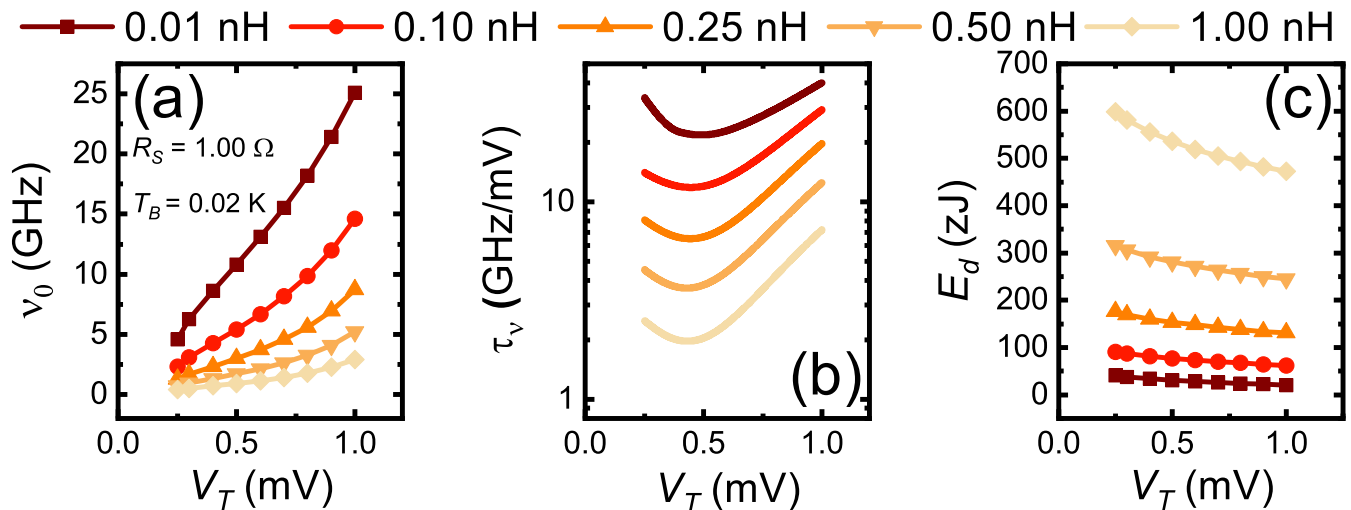


FIG. 4. Figures of merit of the QUISTRON vs. V_T for different shunt inductors L_S , with fixed $R_S = 1.00 \Omega$ and $T_B = 0.02 \text{ K}$. (a) Inverse of oscillation period ν_0 vs. V_T . ν_0 increases monotonically with V_T . Larger L_S decreases ν_0 due to increased characteristic time of the RL circuit formed by nanowire and shunt. (b) Frequency to voltage transfer function τ_ν , obtained by deriving the cubic spline of data in (a) for V_T . (c) Total energy dissipated per period E_d , calculated by integrating over the oscillation period $T = 1/\nu_0$ the sum of absolute values of all heat currents, Joule power, and energy in every inductor and capacitor.

the one dissipated while in the superconducting state (see Appendix C for details in its estimation). We measured E_d values of around 100 zJ, remarkably low and similar to those obtained in other superconducting electronic devices like RFSQ [3], the state-of-the-art for low-dissipation electronics.

It is worth highlighting the relationship between the oscillation frequency and the total energy dissipation per cycle (E_d). As the oscillation frequency increases, we notice that E_d monotonically decreases. This result can be explained by considering the power consumption and the oscillation period. The device power consumption remains almost constant as we change L_S . A slight decrease is due to lower inductance energy, but this contribution is overall negligible. As the frequency increases, the period of each oscillation cycle decreases. E_d is calculated by integrating the power consumed over one oscillation period. With a faster oscillation (shorter period) and nearly constant power consumption, we are integrating over a shorter time interval. As a result, a higher frequency leads to lower energy dissipation per cycle, even though the average power consumption remains relatively constant. As shown in Fig. 4, the shunt inductance dramatically affects the device performance. By varying the inductance from 1 nH to 0.01 nH, ν_0 and τ_ν change by an order of magnitude. It is possible to adjust the oscillation frequency of the device from about 400 MHz to approximately 25 GHz by using a variable shunt inductor, such as by utilizing a SQUID or the kinetic inductance of another nanowire. This device covers all the necessary ranges for microwave applications, especially the 1-10 GHz range, which is important for quantum information applications.

Figure 5 illustrates the device characteristics for different R_S values, with fixed $L_S = 0.25 \text{ nH}$ and $T_B = 0.02 \text{ K}$. In Fig. 5(a), we see that ν_0 increases monotonically with V_T for all R_S values. However, in contrast to the effect of L_S , larger R_S values lead to higher ν_0 for a given V_T . This is due to the shorter characteristic time of the RL circuit when R_S is increased, resulting in faster current redistribution and, consequently, higher oscillation frequencies.

The frequency-to-voltage transfer function τ_ν for varying R_S is shown in Fig. 5(b), calculated using the same method as in Fig. 4(b). The differences in τ_ν across different R_S values indicate how the shunt resistance affects the device frequency tunability. Fig. 5(c) shows the total energy dissipated per period, E_d , for different R_S values. As already shown in Fig. 4(c), in this case, we also obtained values of E_d on the order of 100 zJ, with a monotonically decreasing E_d as the oscillation frequency increases. However, as R_S increases, so does the Joule heating, resulting in greater dissipated power. Indeed, another effect of the value of the shunt resistor R_S is to change the parallel resistance of the circuit, which in turn affects the amplitude of the V_{out} spikes and the Joule heating of the nanowire. For larger R_S , both these quantities increase. If R_S becomes too large, the Joule heating in the nanowire cannot be efficiently dispersed through the cooling fin, and the nanowire electronic temperature would remain higher than the switching temperature T_S even after turning off V_T . This occurs for shunt resistors larger than 1.25Ω . In such cases, once the nanowire is heated above T_S by the quasiparticle injection, it oscillates even after V_T is turned to 0 V.

The results presented in Fig. 4 and Fig. 5 demonstrate

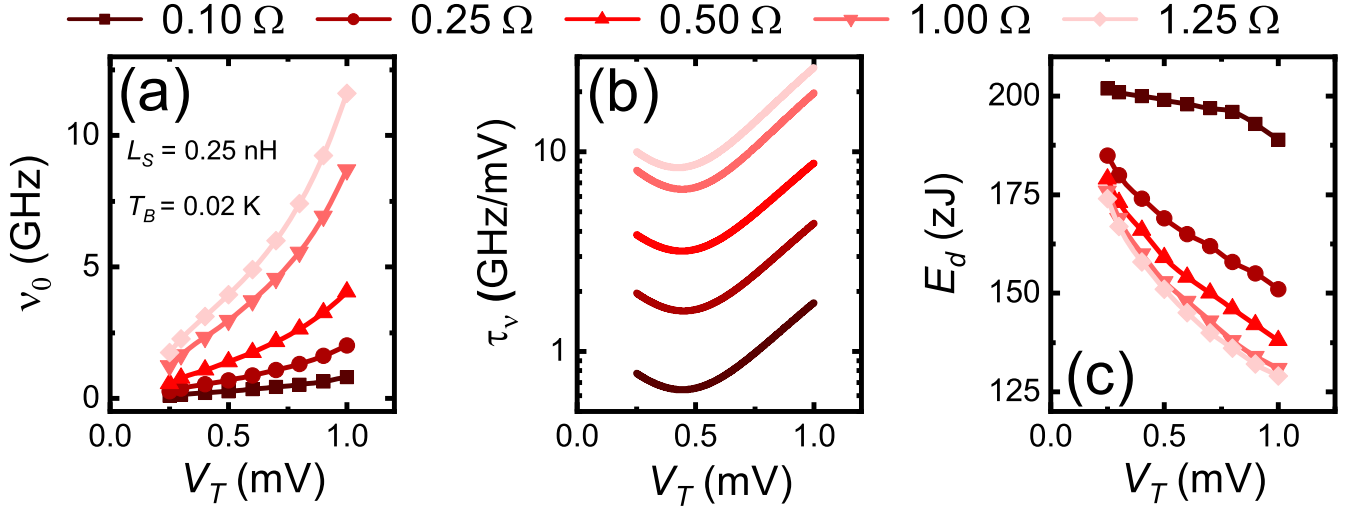


FIG. 5. Figures of merit of the QUISTRON vs. V_T for different shunt resistors R_S , with fixed $L_S = 0.25$ nH and $T_B = 0.02$ K. (a) Inverse of oscillation period ν_0 vs. V_T . ν_0 increases monotonically with V_T . Larger R_S increases ν_0 due to the shorter characteristic time of the RL circuit formed by nanowire and shunt. (b) Frequency to voltage transfer function τ_ν , obtained by deriving the cubic spline of data in (a) for V_T . (c) Total energy dissipated per period E_d , calculated by integrating over the oscillation period $T = 1/\nu_0$ the sum of absolute values of all heat currents, Joule power, and energy in every inductor and capacitor.

that both L_S and R_S play crucial roles in determining the performance characteristics of the QUISTRON. The shunt inductance primarily affects the oscillation frequency by modulating the characteristic time of the RL circuit. In contrast, the shunt resistance influences the frequency, the amplitude of V_{out} , and the power consumption. These findings provide valuable insights for optimizing the device performance for specific applications. For instance, if a higher oscillation frequency is desired, one could opt for a lower L_S or a higher R_S . Furthermore, the voltage-dependent behavior of ν_0 , τ_ν , and E_d across different L_S and R_S values suggests that the device operating point can be finely tuned to meet specific requirements in terms of frequency, sensitivity, and energy efficiency. This flexibility makes the QUISTRON a versatile component for various superconducting electronic applications.

C. Impact of bath temperature

The performance of the QUISTRON is significantly influenced by the operating temperature. To investigate this dependence, we analyzed the device characteristics across a range of bath temperatures (T_B) from 0.02 K to 1.00 K. Figure 6 illustrate the effects of temperature on the NIS (Normal metal-Insulator-Superconductor) tunnel junction characteristics and the nanowire switching current.

In Fig. 6(a), we observe the charge current (I_T) versus applied voltage (V_T) characteristics. At low T_B , the subgap current is negligible, indicating effective electrical isolation. A sharp increase in current occurs at $V_T \simeq$

$\Delta_1/e = 0.2$ mV, where Δ_1 is the superconducting gap energy. As T_B increases, the I-V curves become smoother, and the subgap current rises due to the thermal excitation of quasiparticles. The heat current P_T^{NIS} versus V_T curves in Fig. 6(b) show similar temperature-dependent behavior. At low T_B , there is thermal isolation for subgap voltages. Higher bath temperatures lead to increased heat flow and smoother curves. Figure 6(c) illustrates the nanowire switching current (I_S) versus V_T , which is critical for device operation. At $T_B = 0.02$ K, I_S drops sharply at $V_T \simeq \Delta_1/e = 0.2$ mV, corresponding to the sharp increase in heat current near Δ_1/e . As T_B increases, these curves become smoother, mirroring the behavior of the heat current curves in Fig. 6(b). The dashed black line indicates the bias current I_{bias} used in simulations. It was chosen to be smaller than the switching current at 1 K to use the same bias current in each simulation. It should be noted that this choice of bias current is not optimal for every bath temperature because a lower bias current than the switching current means that a larger injected power is needed to activate the oscillation, thus decreasing the efficiency of the device.

The results presented in Fig. 6 and Fig. 7 show the impact of bath temperature on the device. The temperature-dependent behavior of the NIS junction, particularly the smoothing of $I - V$ characteristics and the shift in nanowire switching current, directly influences the device operating range and performance. The device can operate at lower voltages and bias currents at higher temperatures, which could be advantageous for low-power applications. However, this comes at the cost of increased subgap currents and heat

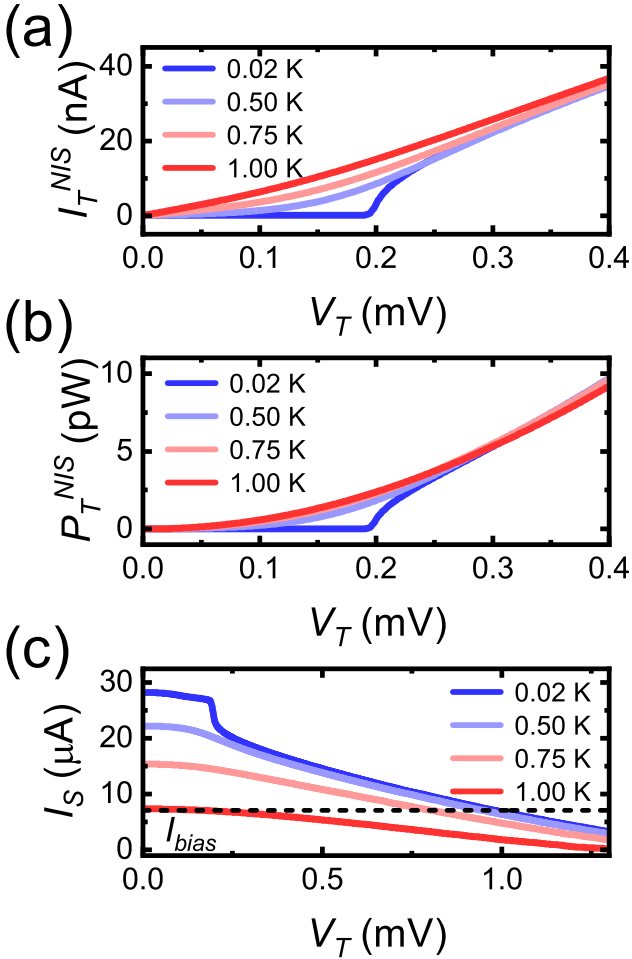


FIG. 6. Impact of bath temperature T_B (ranging from 0.02 K to 1.00 K) on a NIS (normal metal-insulator-superconductor) tunnel junction characteristics and the associated nanowire switching current (I_S). (a) Charge current (I_T^{NIS}) vs. applied voltage (V_T) curves. At low T_B , the subgap current is negligible, showing electrical isolation. Current increases rapidly at $V_T \simeq \Delta_1/e = 0.2$ mV, where Δ_1 is the superconducting gap energy. Higher T_B smooths the curves and increases the subgap current due to thermal quasiparticle excitation. (b) Heat current through the NIS junction P_T^{NIS} vs. V_T curves, showing thermal isolation at low T_B for subgap voltages and increased heat flow and smoother curves at higher T_B . (c) Nanowire switching current (I_S) vs. V_T curves, critical for device operation. At $T_B = 0.02$ K, I_S drops sharply at $V_T \simeq \Delta_1/e = 0.2$ mV due to the sharp increase in heat current near Δ_1/e . Higher T_B smooths these curves, mirroring the smoothing of the heat current vs. V_T curves in (b). Dashed black line indicates I_{bias} used in simulations shown in Fig. 7.

flow, potentially affecting the device energy efficiency. The temperature dependence of ν_0 , τ_ν , and E_d suggests that the device is robust and predictable under bath temperature variations, as its functioning was simulated up to a bath temperature of $T_B = 1$ K. In addition, this temperature sensitivity could be exploited in specific

applications, such as bolometry or temperature sensing.

Figure 7 presents the device figures of merit as functions of V_T for different bath temperatures, with fixed $L_S = 0.25$ nH and $R_S = 1.00$ Ω . Fig. 7(a) shows that the inverse of the oscillation period (ν_0) increases monotonically with V_T for all T_B . However, higher bath temperatures shift the nanowire operation voltage towards lower values. This shift occurs because less voltage (and power) is needed to reduce the switching current below the bias current at higher T_B , as evidenced by the I_S vs. V_T curves in Fig. 6(c). The frequency-to-voltage transfer function (τ_ν), shown in Fig. 7(b), is obtained by calculating the derivative of a cubic spline fit to the data in Fig. 7(a) for V_T . The temperature dependence of τ_ν shows how the device frequency tunability changes with bath temperature. As already seen in Fig. 7(a), the bath temperature main effect is shifting the nanowire operation voltage towards lower values.

Notably, the largest swing in τ_ν is obtained at $T_B = 1$ K. The reason is that the bias current chosen to perform the simulation is slightly lower than the switching current at 1 K, as shown in Fig. 6(c). This is the optimal configuration for the device because it allows for a low switching voltage and large operation voltages. Figure 7(c) presents the total energy dissipated per period (E_d) as a function of V_T for different T_B . We calculated E_d by integrating the sum of absolute values of all heat currents, Joule power, and energy in every inductor and capacitor over one oscillation period $T = 1/\nu_0$.

As the bath temperature T_B increases, we observe a decrease in the total energy dissipated per period, E_d . This inverse relationship can be attributed to the reduced power required from the quasiparticle-injection tunnel junction to switch the nanowire. The reduction in power requirement stems from the decrease in switching current with increasing T_B . However, this analysis does not fully capture an essential aspect of the device behavior: the decrease in voltage swing as T_B increases, a phenomenon previously explained and illustrated in Fig. 3. While the device remains operational at higher temperatures, this temperature dependence has significant implications for its performance. Specifically, the AC power output of the device decreases with increasing T_B .

V. CONCLUSIONS

In conclusion, our investigations demonstrate the potential of an original relaxation oscillator design: the QUISTRON. This device comprises a superconducting nanowire shunted by a resistor and an inductor, with its operation controlled by a voltage applied to a tunnel junction positioned on the nanowire. The oscillation frequency is modulated via a DC voltage applied to a normal metal-insulator-superconductor (NIS) tunnel junction, inducing quasiparticle injection and localized

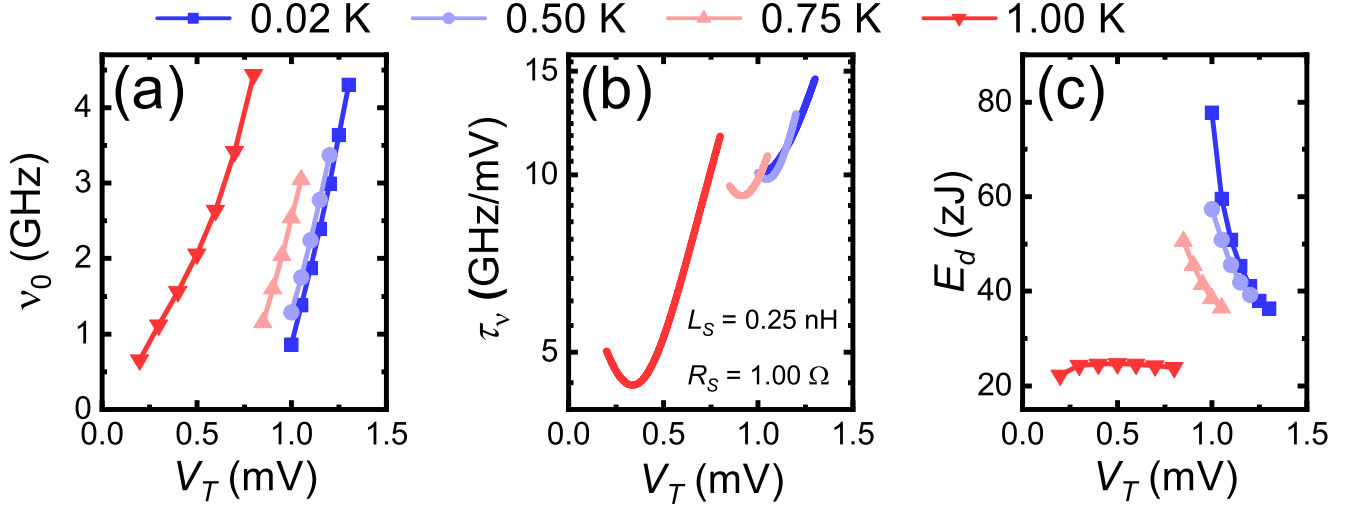


FIG. 7. Figures of merit of the QUISTRON vs. V_T for different bath temperatures T_B , with fixed $L_S = 0.25$ nH and $R_S = 1.00$ Ω . (a) Inverse of oscillation period ν_0 vs. V_T . ν_0 increases monotonically with V_T . Higher T_B shifts nanowire operation voltage towards lower values, as less voltage (and power) is needed to reduce switching current below bias current at higher T_B . (b) Frequency to voltage transfer function τ_ν , obtained by deriving the cubic spline of data in (a) for V_T . (c) Total energy dissipated per period E_d , calculated by integrating over the oscillation period $T = 1/\nu_0$ the sum of absolute values of all heat currents, Joule power, and energy in every inductor and capacitor.

heating of the nanowire. This mechanism effectively modulates the nanowire switching current, initiating oscillations when it falls below a DC bias current.

Numerical simulations have confirmed the device functionality and explored its performance characteristics. The results are promising, revealing an oscillation frequency range of 1.2 GHz to 8.7 GHz—ideal for microwave applications for a specific configuration of shunt resistor and inductor ($R_S = 1$ Ω , $L_S = 0.25$ nH). Moreover, the QUISTRON exhibits ultra-low energy dissipation of ~ 100 zJ per cycle and maintains operational stability across a broad temperature range (20 mK to 1 K). These attributes underscore the QUISTRON potential as a compact, tunable, and localized superconducting oscillator. Its straightforward DC voltage control mechanism and compatibility with circuit integration render it a compelling candidate for diverse applications in quantum information processing, microwave technology, and ultra-low-power electronics.

Notably, any mechanism to decrease the switching current in a superconducting channel shunted by a resistor could be exploited to design a superconducting

relaxation oscillator. Alternative architectures for voltage-controlled superconducting relaxation oscillators could be developed using different principles. These include superconductor-normal metal-superconductor (SNS) junctions with semiconducting channels controlled by gating effects [65, 66] and gate-controlled superconductivity in metallic superconductors [67, 68]. Such diverse approaches highlight the rich potential for innovation in superconducting relaxation oscillators. Future research endeavors will focus on experimentally validating the proposed design and further optimizing its performance characteristics.

ACKNOWLEDGEMENTS

We acknowledge the EU’s Horizon 2020 Research and Innovation Framework Programme under Grants No. 964398 (SUPERGATE), No. 101057977 (SPECTRUM), and the PNRR MUR project PE0000023-NQSTI for partial financial support.

[1] A. Blais, A. L. Grimsmo, S. M. Girvin, and A. Wallraff, Circuit quantum electrodynamics, *Rev. Mod. Phys.* **93**, 025005 (2021).
 [2] M. H. Devoret and R. J. Schoelkopf, Superconducting circuits for quantum information: An outlook, *Science* **339**, 1169 (2013).
 [3] K. Likharev and V. Semenov, RSFQ logic/memory family: a new Josephson-junction technology

for sub-terahertz-clock-frequency digital systems, *IEEE Trans. Appl. Supercond.* **1**, 3 (1991).
 [4] O. A. Mukhanov, Energy-efficient single flux quantum technology, *IEEE Trans. Appl. Supercond.* **21**, 760 (2011).
 [5] O. Chen, R. Cai, Y. Wang, F. Ke, T. Yamae, R. Saito, N. Takeuchi, and N. Yoshikawa, Adiabatic Quantum-Flux-Parametron: Towards Building

- Extremely Energy-Efficient Circuits and Systems, *Sci. Rep.* **9**, 10514 (2019).
- [6] K. D. Irwin, An application of electrothermal feedback for high resolution cryogenic particle detection, *Appl. Phys. Lett.* **66**, 1998 (1995).
- [7] G. Gol'tsman, O. Okunev, G. Chulkova, A. Lipatov, A. Semenov, K. Smirnov, B. Voronov, A. Dzardanov, G. Williams, and R. Sobolewski, Picosecond superconducting single photon optical detector, *Appl. Phys. Lett.* **78**, 705 (2001).
- [8] P. K. Day, H. G. LeDuc, B. A. Mazin, A. Vayonakis, and J. Zmuidzinas, A broadband superconducting detector suitable for use in large arrays, *Nature* **425**, 817 (2003).
- [9] F. Giazotto, T. T. Heikkilä, G. P. Pepe, P. Heliö, A. Luukanen, and J. P. Pekola, Ultrasensitive proximity josephson sensor with kinetic inductance readout, *Appl. Phys. Lett.* **92** (2008).
- [10] C. Guarcello, A. Braggio, P. Solinas, G. P. Pepe, and F. Giazotto, Josephson-threshold calorimeter, *Phys. Rev. Appl.* **11**, 054074 (2019).
- [11] P. Krantz, M. Kjaergaard, F. Yan, T. P. Orlando, S. Gustavsson, and W. D. Oliver, A quantum engineer's guide to superconducting qubits, *Appl. Phys. Rev.* **6**, 021318 (2019).
- [12] Y. Chen *et al.*, Qubit architecture with high coherence and fast tunable coupling, *Phys. Rev. Lett.* **113**, 220502 (2014).
- [13] D. Crankshaw, J. Habif, X. Zhou, T. Orlando, M. Feldman, and M. Bocko, An rsfq variable duty cycle oscillator for driving a superconductive qubit, *IEEE Trans. Appl. Supercond.* **13**, 966 (2003).
- [14] Z. Bao, Y. Li, Z. Wang, J. Wang, J. Yang, H. Xiong, Y. Song, Y. Wu, H. Zhang, and L. Duan, A cryogenic on-chip microwave pulse generator for large-scale superconducting quantum computing, *Nat. Commun.* **15**, 5958 (2024).
- [15] K. Gaj, E. Friedman, M. Feldman, and A. Krasniewski, A clock distribution scheme for large rsfq circuits, *IEEE Trans. Appl. Supercond.* **5**, 3320 (1995).
- [16] S. Buchman, J. Turneaure, J. Lipa, M. Dong, K. Cumbermack, and S. Wang, A superconducting microwave oscillator clock for use on the space station, in *Proc. IEEE Intl. Freq. Cont. Symp. (Cat. No.98CH36165)* (1998) pp. 534–539.
- [17] V. P. Koshelets and S. V. Shitov, Integrated superconducting receivers, *Supercond. Sci. Technol.* **13**, R53 (2000).
- [18] M. A. Galin, A. M. Klushin, V. V. Kurin, S. V. Seliverstov, M. I. Finkel, G. N. Goltsman, F. Müller, T. Scheller, and A. D. Semenov, Towards local oscillators based on arrays of niobium Josephson junctions, *Supercond. Sci. Technol.* **28**, 055002 (2015).
- [19] S. Benz and P. Booi, High-frequency oscillators using phase-locked arrays of josephson junctions, *IEEE Trans. Ultrason. Ferroelectr. Freq. Control* **42**, 964 (1995).
- [20] D. Niepce, J. Burnett, and J. Bylander, High kinetic inductance NbN nanowire superinductors, *Phys. Rev. Appl.* **11**, 044014 (2019).
- [21] S. Frasca, I. Arabadzhiev, S. B. de Puechredon, F. Oppliger, V. Jouanny, R. Musio, M. Scigliuzzo, F. Minganti, P. Scarlino, and E. Charbon, Nbn films with high kinetic inductance for high-quality compact superconducting resonators, *Phys. Rev. Appl.* **20**, 044021 (2023).
- [22] P. Kamenov, W.-S. Lu, K. Kalashnikov, T. DiNapoli, M. T. Bell, and M. E. Gershenson, Granular aluminum meandered superinductors for quantum circuits, *Phys. Rev. Appl.* **13**, 054051 (2020).
- [23] T. M. Hazard, A. Gyenis, A. Di Paolo, A. T. Asfaw, S. A. Lyon, A. Blais, and A. A. Houck, Nanowire superinductance fluxonium qubit, *Phys. Rev. Lett.* **122**, 010504 (2019).
- [24] A. J. Annunziata, D. F. Santavica, L. Frunzio, G. Catelani, M. J. Rooks, A. Frydman, and D. E. Prober, Tunable superconducting nanoinductors, *Nanotechnol.* **21**, 445202 (2010).
- [25] M. R. Vissers, J. Hubmayr, M. Sandberg, S. Chaudhuri, C. Bockstiegel, and J. Gao, Frequency-tunable superconducting resonators via nonlinear kinetic inductance, *Appl. Phys. Lett.* **107**, 062601 (2015).
- [26] M. Khalifa and J. Salfi, Nonlinearity and parametric amplification of superconducting nanowire resonators in magnetic field, *Phys. Rev. Appl.* **19**, 034024 (2023).
- [27] C. Joshi, W. Chen, H. G. LeDuc, P. K. Day, and M. Mirhosseini, Strong kinetic-inductance kerr nonlinearity with titanium nitride nanowires, *Phys. Rev. Appl.* **18**, 064088 (2022).
- [28] J. P. Allmaras, A. G. Kozorezov, A. D. Beyer, F. Marsili, R. M. Briggs, and M. D. Shaw, Thin-Film Thermal Conductivity Measurements Using Superconducting Nanowires, *J. Low Temp. Phys.* **193**, 380 (2018).
- [29] A. Dane, J. Allmaras, D. Zhu, M. Onen, M. Colangelo, R. Baghdadi, J.-L. Tambasco, Y. Morimoto, I. E. Forno, I. Charaev, Q. Zhao, M. Skvortsov, A. Kozorezov, and K. K. Berggren, Self-heating hotspots in superconducting nanowires cooled by phonon black-body radiation, *Nat. Commun.* **13**, 5429 (2022).
- [30] F. Giazotto, T. T. Heikkilä, A. Luukanen, A. M. Savin, and J. P. Pekola, Opportunities for mesoscopics in thermometry and refrigeration: Physics and applications, *Rev. Mod. Phys.* **78**, 217 (2006).
- [31] A. Fornieri and F. Giazotto, Towards phase-coherent caloritronics in superconducting circuits, *Nat. Nanotechnol.* **12**, 944 (2017).
- [32] R. Kokkonen, J.-P. Girard, D. Hazra, A. Laitinen, J. Govenius, R. E. Lake, I. Sallinen, V. Vesterinen, M. Partanen, J. Y. Tan, K. W. Chan, K. Y. Tan, P. Hakonen, and M. Möttönen, Bolometer operating at the threshold for circuit quantum electrodynamics, *Nature* **586**, 47 (2020).
- [33] A. M. Gunyhó, S. Kundu, J. Ma, W. Liu, S. Niemelä, G. Catto, V. Vadimov, V. Vesterinen, P. Singh, Q. Chen, and M. Möttönen, Single-shot readout of a superconducting qubit using a thermal detector, *Nat. Electron.* **7**, 288 (2024).
- [34] F. Paolucci, V. Buccheri, G. Germanese, N. Ligato, R. Paoletti, G. Signorelli, M. Bitossi, P. Spagnolo, P. Falferi, M. Rajteri, C. Gatti, and F. Giazotto, Development of highly sensitive nanoscale transition edge sensors for gigahertz astronomy and dark matter search, *J. Appl. Phys.* **128**, 194502 (2020).
- [35] F. Paolucci, N. Ligato, G. Germanese, V. Buccheri, and F. Giazotto, Fully Superconducting Josephson Bolometers for Gigahertz Astronomy, *Appl. Sci.* **11**, 10.3390/app11020746 (2021).
- [36] A. Shurakov, Y. Lobanov, and G. Goltsman, Superconducting hot-electron bolometer: from the discovery of hot-electron

- phenomena to practical applications, *Supercond. Sci. Technol.* **29**, 023001 (2015).
- [37] B. Korzh *et al.*, Demonstration of sub-3 ps temporal resolution with a superconducting nanowire single-photon detector, *Nat. Photon.* **14**, 250 (2020).
- [38] F. Grünenfelder, A. Boaron, G. V. Resta, M. Perrenoud, D. Rusca, C. Barreiro, R. Houlmann, R. Sax, L. Stasi, S. El-Khoury, E. Hänggi, N. Bosshard, F. Bussi eres, and H. Zbinden, Fast single-photon detectors and real-time key distillation enable high secret-key-rate quantum key distribution systems, *Nat. Photon.* **17**, 422 (2023).
- [39] I. Charaev, E. K. Batson, S. Cherednichenko, K. Reidy, V. Drakinskiy, Y. Yu, S. Lara-Avila, J. D. Thomsen, M. Colangelo, F. Incalza, K. Ilin, A. Schilling, and K. K. Berggren, Single-photon detection using large-scale high-temperature MgB2 sensors at 20 K, *Nat. Commun.* **15**, 3973 (2024).
- [40] S. Faris, S. Raider, W. Gallagher, and R. Drake, Quiteron, *IEEE Trans. Magn.* **19**, 1293 (1983).
- [41] N. E. Booth, P. A. Fisher, M. Nahum, and J. N. Ullom, The quatratron, *Nucl. Instrum. Methods Phys. Res. A* **444**, 33 (2000).
- [42] A. N. McCaughan and K. K. Berggren, A Superconducting-Nanowire Three-Terminal Electrothermal Device, *Nano Lett.* **14**, 5748 (2014).
- [43] R. Baghdadi, J. P. Allmaras, B. A. Butters, A. E. Dane, S. Iqbal, A. N. McCaughan, E. A. Toomey, Q.-Y. Zhao, A. G. Kozorezov, and K. K. Berggren, Multilayered Heater Nanocryotron: A Superconducting-Nanowire-Based Thermal Switch, *Phys. Rev. Appl.* **14**, 054011 (2020).
- [44] A. Buzzi, M. Castellani, R. A. Foster, O. Medeiros, M. Colangelo, and K. K. Berggren, A nanocryotron memory and logic family, *Appl. Phys. Lett.* **122**, 142601 (2023).
- [45] E. Toomey, K. Segall, and K. K. Berggren, Design of a Power Efficient Artificial Neuron Using Superconducting Nanowires, *Frontiers in Neuroscience* **13**, 933 (2019).
- [46] E. Toomey, K. Segall, M. Castellani, M. Colangelo, N. Lynch, and K. K. Berggren, Superconducting Nanowire Spiking Element for Neural Networks, *Nano Lett.* **20**, 8059 (2020).
- [47] A. E. Lombo, J. Lares, M. Castellani, C.-N. Chou, N. Lynch, and K. K. Berggren, A superconducting nanowire-based architecture for neuromorphic computing, *Neuromorph. Comput. Eng.* **2**, 034011 (2022).
- [48] E. Toomey, Q.-Y. Zhao, A. N. McCaughan, and K. K. Berggren, Frequency Pulling and Mixing of Relaxation Oscillations in Superconducting Nanowires, *Phys. Rev. Appl.* **9**, 064021 (2018).
- [49] E. Toomey, Microwave Response of Nonlinear Oscillations in Resistively Shunted Superconducting Nanowires (2017).
- [50] F. Giazotto and J. P. Pekola, Josephson tunnel junction controlled by quasiparticle injection, *J. Appl. Phys.* **97**, 10.1063/1.1833576 (2005).
- [51] S. A. Lemziakov, B. Karimi, S. Nakamura, D. S. Lvov, R. Upadhyay, C. D. Satrya, Z.-Y. Chen, D. Subero, Y.-C. Chang, L. B. Wang, and J. P. Pekola, Applications of Superconductor–Normal Metal Interfaces, *J. Low Temp. Phys.* 10.1007/s10909-024-03144-8 (2024).
- [52] S. Tirelli, A. Savin, C. P. Garcia, J. P. Pekola, F. Beltram, and F. Giazotto, Manipulation and generation of supercurrent in out-of-equilibrium josephson tunnel nanojunctions, *Phys. Rev. Lett.* **101**, 077004 (2008).
- [53] L. J. Splitthoff, J. J. Wesdorp, M. Pita-Vidal, A. Bargerbos, Y. Liu, and C. K. Andersen, Gate-tunable kinetic inductance parametric amplifier, *Phys. Rev. Appl.* **21**, 014052 (2024).
- [54] T. M. Lanting, H.-M. Cho, J. Clarke, W. L. Holzapfel, A. T. Lee, M. Lueker, P. L. Richards, M. A. Dobbs, H. Spieler, and A. Smith, Frequency-domain multiplexed readout of transition-edge sensor arrays with a superconducting quantum interference device, *Appl. Phys. Lett.* **86**, 112511 (2005).
- [55] H. Sipola, J. Luomahaara, A. Timofeev, L. Gr onberg, A. Rautiainen, A. Luukanen, and J. Hassel, Multiplexed readout of kinetic inductance bolometer arrays, *Rev. Sci. Instrum.* **90**, 074702 (2019).
- [56] P. D. Mauskopf, Transition Edge Sensors and Kinetic Inductance Detectors in Astronomical Instruments, *Publ. Astron. Soc. Pac.* **130**, 082001 (2018).
- [57] D. Sandgren, D. Chouvaev, M. Tarasov, and L. Kuzmin, Fabrication and optical characterization of the normal metal hot-electron microbolometer with Andreev mirrors, *Phys. C: Supercond. Appl* **372-376**, 444 (2002).
- [58] J. Bardeen, Critical fields and currents in superconductors, *Rev. Mod. Phys.* **34**, 667 (1962).
- [59] J. Romijn, T. M. Klapwijk, M. J. Renne, and J. E. Mooij, Critical pair-breaking current in superconducting aluminum strips far below T_c , *Phys. Rev. B* **26**, 3648 (1982).
- [60] V. Ambegaokar and A. Baratoff, Tunneling between superconductors, *Phys. Rev. Lett.* **10**, 486 (1963).
- [61] M. Tinkham, *Introduction to Superconductivity*, 2nd ed. (Dover Publications, 2004).
- [62] F. Gross, B. S. Chandrasekhar, D. Einzel, K. Andres, P. J. Hirschfeld, H. R. Ott, J. Beuers, Z. Fisk, and J. L. Smith, Anomalous temperature dependence of the magnetic field penetration depth in superconducting UBe13, *Z. Phys. B* **64**, 175 (1986).
- [63] S. V. Lotkhov, E. M. Tolkacheva, D. V. Balashov, M. I. Khabipov, F.-I. Buchholz, and A. B. Zorin, Low hysteretic behavior of Al/AlOx/Al Josephson junctions, *Appl. Phys. Lett.* **89**, 132115 (2006).
- [64] K. D. Usadel, Generalized diffusion equation for superconducting alloys, *Phys. Rev. Lett.* **25**, 507 (1970).
- [65] J. Shabani, M. Kjaergaard, H. J. Suominen, Y. Kim, F. Nichele, K. Pakrouski, T. Stankevici, R. M. Lutchyn, P. Krogstrup, R. Feidenhans'l, S. Kraemer, C. Nayak, M. Troyer, C. M. Marcus, and C. J. Palmstr om, Two-dimensional epitaxial superconductor-semiconductor heterostructures: A platform for topological superconducting networks, *Phys. Rev. B* **93**, 155402 (2016).
- [66] K. Aggarwal, A. Hofmann, D. Jirovec, I. Prieto, A. Sammak, M. Botifoll, S. Mart ı-S anchez, M. Veldhorst, J. Arbiol, G. Scappucci, J. Danon, and G. Katsaros, Enhancement of proximity-induced superconductivity in a planar ge hole gas, *Phys. Rev. Res.* **3**, L022005 (2021).
- [67] G. De Simoni, F. Paolucci, P. Solinas, E. Strambini, and F. Giazotto, Metallic supercurrent field-effect transistor, *Nat. Nanotechnol.* **13**, 802 (2018).
- [68] F. Paolucci, G. De Simoni, P. Solinas, E. Strambini, C. Puglia, N. Ligato, and F. Giazotto, Field-effect control of metallic superconducting systems,

- AVS Quantum Sci. **1**, 016501 (2019).
- [69] J. P. Pekola, T. Heikkilä, A. Savin, J. Flyktman, F. Giazotto, and F. Hekking, Limitations in cooling electrons using normal-metal-superconductor tunnel junctions, *Phys. Rev. Lett.* **92**, 056804 (2004).
- [70] A. M. Savin, J. P. Pekola, J. T. Flyktman, A. Anthore, and F. Giazotto, Cold electron Josephson transistor, *Appl. Phys. Lett.* **84**, 4179 (2004).
- [71] M. Meschke, J. P. Pekola, F. Gay, R. E. Rapp, and H. Godfrin, Electron Thermalization in Metallic Islands Probed by Coulomb Blockade Thermometry, *J. Low Temp. Phys.* **134**, 1119 (2004).
- [72] A. Timofeev, C. P. Garcia, N. Kopnin, A. Savin, M. Meschke, F. Giazotto, and J. Pekola, Recombination-limited energy relaxation in a bardeen-cooper-schrieffer superconductor, *Phys. Rev. Lett.* **102**, 017003 (2009).
- [73] V. F. Maisi, S. V. Lotkhov, A. Kemppinen, A. Heimes, J. T. Muhonen, and J. P. Pekola, Excitation of single quasiparticles in a small superconducting island connected to normal-metal leads by tunnel junctions, *Phys. Rev. Lett.* **111**, 147001 (2013).
- [74] W. J. Skocpol, M. R. Beasley, and M. Tinkham, Self-heating hotspots in superconducting thin-film microbridges, *J. Appl. Phys.* **45**, 4054 (1974).
- [75] M. Tinkham, J. U. Free, C. N. Lau, and N. Markovic, Hysteretic I - V curves of superconducting nanowires, *Phys. Rev B* **68**, 134515 (2003).
- [76] S. Battisti, J. Koch, A. Paghi, L. Ruf, A. Gulian, S. Teknowijoyo, C. Cirillo, Z. M. Kakhaki, C. Attanasio, E. Scheer, A. Di Bernardo, G. De Simoni, and F. Giazotto, Demonstration of high-impedance superconducting NbRe Dayem bridges, *Appl. Phys. Lett.* **124**, 172601 (2024).

Appendix A: Estimation of heat currents

The injection junction charge and heat currents flowing into the nanowire when it is superconducting, shown in Fig. 1(b), are expressed by [30]:

$$I_T^{NIS} = \frac{1}{eR_T} \int_{-\infty}^{\infty} d\epsilon \mathcal{N}_{S_1}(\epsilon, T_{el}) \times [f_0(\epsilon - eV_T, T_B) - f_0(\epsilon, T_{el})], \quad (\text{A1})$$

$$P_T^{NIS} = \frac{1}{e^2 R_T} \int_{-\infty}^{\infty} d\epsilon \epsilon \mathcal{N}_{S_1}(\epsilon, T_{el}) \times [f_0(\epsilon - eV_T, T_B) - f_0(\epsilon, T_{el})], \quad (\text{A2})$$

where e is the elementary charge, R_T is the tunnel junction resistance, V_T is the voltage applied to the junction, T_{el} is the electronic temperature of the nanowire, T_B is the bath temperature, $f_0(E, T) = 1/[\exp(E/k_B T) + 1]$ is the Fermi-Dirac distribution of the quasiparticles at energy E and electronic temperature T , and $\mathcal{N}_{S_1}(E, T) = \left| \Re \left[E + i\Gamma_1 / \sqrt{(E + i\Gamma_1)^2 - \Delta_1^2(T)} \right] \right|$ is the (smeared by the Dynes parameter $\Gamma_1 = 10^{-3}\Delta_1$) BCS density of states (DOS) of the S_1 superconductor normalized at the Fermi level [69]. The charge and

heat current when the nanowire is in the normal state, respectively I_T^{NIN} and P_T^{NIN} , are the same expressions in which the normalized DOS is set to be normal metal one, which is constantly equal to 1. The cooling fin junction heat current flowing out of the nanowire when it is in the superconducting is expressed by:

$$P_C^{NIS} = -\frac{1}{e^2 R_C} \int_{-\infty}^{\infty} d\epsilon \epsilon \mathcal{N}_{S_1}(\epsilon, T_{el}) \times [f_0(\epsilon, T_B) - f_0(\epsilon, T_{el})], \quad (\text{A3})$$

where R_C is the tunnel junction resistance. The heat current when the nanowire is in the normal state, P_C^{NIN} , is given by the same expression with the normalized DOS set to that of a normal metal, which is constantly equal to 1. The absence of a superconducting gap, which exponentially suppresses the subgap DOS, amplifies the heat current flowing in the cooling fin while the nanowire is in the normal state, introducing a feedback control on the electronic temperature of the nanowire that depends on its state.

The lateral banks junction heat current flowing out of the nanowire when it is superconducting is expressed by [30]:

$$2P_J^{SIS} = -\frac{2}{e^2 R_J} \int_{-\infty}^{\infty} d\epsilon \epsilon \mathcal{N}_{S_1}(\epsilon, T_{el}) \mathcal{N}_{S_2}(\epsilon, T_B) \times [f_0(\epsilon, T_B) - f_0(\epsilon, T_{el})], \quad (\text{A4})$$

where R_J is the resistance of each tunnel junction, and $\mathcal{N}_{S_2}(E, T) = \left| \Re \left[(E + i\Gamma_2) / \sqrt{(E + i\Gamma_2)^2 - \Delta_2^2(T)} \right] \right|$ is the (smeared by the Dynes parameter $\Gamma_2 = 10^{-3}\Delta_2$) BCS density of states (DOS) of the S_2 superconductor normalized at the Fermi level [69].

When the nanowire is in the normal state, the series of the two junctions and the nanowire effectively acts as a biased SINIS structure. In this case, the heat current also depends on the voltage applied across the structure, particularly on the voltage drop across the two tunnel junctions [30, 50, 70]:

$$P_J^{SINIS} = 2P_J^{NIS} = -\frac{2}{e^2 R_J} \int_{-\infty}^{\infty} d\epsilon \epsilon \mathcal{N}_{S_2}(\tilde{\epsilon}, T_B) \times [f_0(\tilde{\epsilon}, T_B) - f_0(\epsilon, T_{el})], \quad (\text{A5})$$

where $\tilde{\epsilon} = \epsilon - V_{out}(R_J/R_N)$, and $V_{out}(R_J/R_N)$ is the voltage drop across each tunnel junction, which depends on the ratio between the junction resistance R_J and the total series resistance of the two junctions and the nanowire in the normal state $R_N = R_{NW} + 2R_J$.

The heat current flowing out of the nanowire due to the electron-phonon coupling when the nanowire is in the normal state is expressed by [30]:

$$P_{e-ph}^N = \Sigma V (T_{el}^5 - T_B^5), \quad (\text{A6})$$

where Σ is the electron-phonon coupling constant, which for aluminum at sub-Kelvin temperatures is $\Sigma = 0.3 \times 10^9$ W/(m³K⁵) [30, 71], and V is the nanowire volume.

The heat current flowing out of the nanowire due to the electron-phonon coupling when the nanowire is superconducting is expressed by [72, 73]:

$$P_{e-ph}^S = \frac{\Sigma V}{24\zeta(5)k_B^5} \int_0^\infty d\epsilon \epsilon^3 [n(\epsilon, T_{el}) - n(\epsilon, T_B)] \times \int_{-\infty}^\infty dE \mathcal{N}_{S_1}(E, T_{el}) \mathcal{N}_{S_1}(E + \epsilon, T_{el}) \times \left[1 - \frac{\Delta_1^2(T_{el})}{E(E + \epsilon)} \right] [f_0(E, T_{el}) - f_0(E + \epsilon, T_{el})], \quad (\text{A7})$$

where ζ is the Riemann zeta function, $n(\epsilon, T) = 1/[\exp(\epsilon/k_B T) - 1]$ is the Bose-Einstein distribution of the nanowire phonons at energy ϵ and temperature T , and $\Delta_1(T)$ is the nanowire superconducting gap. The superconducting gap suppresses the electron-phonon coupling at low temperatures ($T \ll \Delta_1(T)/k_B$), thus $P_{e-ph}^S < P_{e-ph}^N$.

Appendix B: Estimation of nanowire heat capacity and electron-phonon length

The nanowire electronic heat capacity while in the normal state C_N was estimated as:

$$C_N(T) = \frac{\pi^2}{3} k_B^2 T V D(E_F), \quad (\text{B1})$$

where k_B is the Boltzmann constant, V is the nanowire volume, and $D(E_F) = 1.45 \times 10^{47} \text{ 1/(Jm}^3\text{)}$ is the aluminum density of state at the Fermi energy $E_F = 11.6 \text{ eV}$.

The nanowire electronic heat capacity while in the superconducting state C_S was calculated starting from a fermionic system entropy relation:

$$S(T) = -2k_B \sum_k [f_k \ln(f_k) + (1 - f_k) \ln(1 - f_k)], \quad (\text{B2})$$

where f_k is the Fermi distribution at energy $E = \sqrt{\epsilon_k^2 + \Delta_1^2(T)}$ and temperature T . Then, the heat capacity of a BCS superconductor is [61]:

$$C_S(T) = T \frac{\partial S(T)}{\partial T} = T \sum_k \frac{\partial S}{\partial f_k} \frac{\partial f_k}{\partial T} = \frac{2}{k_B T^2} \sum_k \frac{e^{\frac{\sqrt{\epsilon_k^2 + \Delta_1^2(T)}}{k_B T}}}{\left[e^{\frac{\sqrt{\epsilon_k^2 + \Delta_1^2(T)}}{k_B T}} + 1 \right]^2} \times \left[\epsilon_k^2 + \Delta_1^2(T) - \frac{T}{2} \frac{d}{dT} \Delta_1^2(T) \right], \quad (\text{B3})$$

which in the continuous limit can be written as:

$$C_S(T) = \frac{V D(E_F)}{k_B T^2} \int_{-\infty}^\infty \frac{e^{\frac{\sqrt{\epsilon^2 + \Delta_1^2(T)}}{k_B T}}}{\left[e^{\frac{\sqrt{\epsilon^2 + \Delta_1^2(T)}}{k_B T}} + 1 \right]^2} \times \left[\epsilon^2 + \Delta_1^2(T) - T \Delta_1(T) \frac{d\Delta_1(T)}{dT} \right] d\epsilon. \quad (\text{B4})$$

The nanowire electron-phonon scattering length while in the normal state, l_{e-ph}^N , was estimated as:

$$l_{e-ph}^N = \sqrt{D_{Al} \tau_{e-ph}^N}, \quad (\text{B5})$$

where $D_{Al} = 1/[e^2 \rho_{Al} D(E_F)]$ is the aluminum diffusion constant, ρ_{Al} is the resistivity of an aluminum film 20 nm thick [59], and τ_{e-ph}^N is the electron-phonon scattering time when the nanowire is in the normal state, which is:

$$\tau_{e-ph}^N = \frac{C_N}{G_N}, \quad (\text{B6})$$

$$G_N = \frac{dP_{e-ph}^N}{dT}, \quad (\text{B7})$$

where C_N is the electronic heat capacitance of the nanowire, and G_N is the electron-phonon thermal conductance in the normal state.

The electron-phonon scattering length l_{e-ph}^N is a monotonically decreasing function of temperature. We estimated it at the highest possible operation temperature, which is the critical temperature of the aluminum nanowire $T_{c1} = 1.3 \text{ K}$. It is $l_{e-ph}^N(T_{c1}) \simeq 17 \text{ }\mu\text{m}$, which is much larger than the length of the nanowire $l = 1.2 \text{ }\mu\text{m}$. This means that the temperature dynamics is homogeneous along the entire nanowire while in the normal state.

The nanowire electron-phonon scattering length while in the superconducting state, l_{e-ph}^S , was estimated as:

$$l_{e-ph}^S = \sqrt{D_{Al} \tau_{e-ph}^S}, \quad (\text{B8})$$

where τ_{e-ph}^S is the electron-phonon scattering time when the nanowire is superconducting, which is:

$$\tau_{e-ph}^S = \frac{C_S}{G_S}, \quad (\text{B9})$$

$$G_S = \frac{dP_{e-ph}^S}{dT}. \quad (\text{B10})$$

The electron-phonon scattering length l_{e-ph}^S is a monotonically decreasing function of temperature. We estimated it at the highest possible operation temperature, which is the critical temperature of the aluminum nanowire $T_{c1} = 1.3 \text{ K}$. It is $l_{e-ph}^S(T_{c1}) \simeq 200 \text{ }\mu\text{m}$, which is much larger than the length of the nanowire $l = 1.2 \text{ }\mu\text{m}$. This means that the temperature dynamics is also homogeneous along the entire nanowire while in the superconducting state. These estimations justify the assumption we made to neglect the spatial gradients of the temperature along the nanowire.

Appendix C: Estimation of nanowire retrapping current, kinetic inductance and energy dissipation

The nanowire retrapping current I_R was estimated from the thermal balance between the self-heating due to the Joule power generated while the nanowire is in the normal state and the other heat currents flowing in or from the nanowire, as in [29, 74, 75]. The Joule power dissipated in the nanowire at the retrapping current is $P_{Joule} = [R_{NW} + 2(R_J/2)]I_R^2$, where we assumed that half of the power dissipated on the insulating barriers of resistance R_J is dissipated in the nanowire. Thus, the retrapping current is expressed by the relation:

$$I_R = \sqrt{\frac{P_C^{NIN} + P_J^{SINIS} + P_{e-ph}^N - P_T^{NIN}}{R_{NW} + R_J}}, \quad (C1)$$

where we assumed that the electronic temperature was equal to the critical temperature, as done in [74]. However, this assumption is not completely correct in our device, as we have seen that the actual electronic temperature of the nanowire is variable during the operation, and it is always smaller than T_{c1} .

The device kinetic inductance L_K was estimated as the sum of the nanowire kinetic inductance L_K^{NW} and the two Josephson junctions kinetic inductances L_K^J . We estimated L_K^{NW} from the BCS expression for a superconducting stripe [76]:

$$L_K^{NW}(T) = \frac{\hbar R_{NW}}{\pi \Delta_1(T) \tanh\left[\frac{\Delta_1(T)}{k_B T}\right]}, \quad (C2)$$

while L_K^J was estimated from the linearized Josephson expression:

$$L_K^J(T) = \frac{\Phi_0}{2\pi I_c(T)}, \quad (C3)$$

where $\Phi_0 = \frac{h}{2e} \simeq 2.07$ fWb is the superconducting flux quantum.

The total energy dissipated per cycle E_d was calculated by integrating the sum of the heat currents flowing into the nanowire, Joule power, and energy in every inductor and capacitor over one oscillation period $T = 1/\nu_0$:

$$\begin{aligned} E_d = & \left(\int_0^{t_R} [V_{out}(t)I_{bias} + P_T^{NIN}] dt \right. \\ & + \frac{1}{t_R} \int_0^{t_R} \left[\frac{1}{2} C_J^{eff} V_{out}^2(t) + \frac{1}{2} L_S [I_{bias} - I_{NW}(t)]^2 \right] dt \Big) \\ & + \left(\int_{t_R}^T [V_{out}(t)I_{bias} + P_T^{NIS}] dt \right. \\ & + \frac{1}{T - t_R} \int_{t_R}^T \left[\frac{1}{2} C_J^{eff} V_{out}^2(t) + \frac{1}{2} L_K I_{NW}^2(t) \right. \\ & \left. \left. + \frac{1}{2} L_S [I_{bias} - I_{NW}(t)]^2 \right] dt \right). \quad (C4) \end{aligned}$$

This expression can be divided into the integral of the power dissipated when the nanowire is in the normal state (first two terms) and the power dissipated while in the superconducting state (last two terms), where $C_J^{eff} = (1/C_J + 1/C_J)^{-1} = C_J/2$ is the effective capacitance given by the series of the two junctions between the niobium banks and the aluminum nanowire and t_R is the time during which the nanowire stays in the normal state. This is the time necessary for the current flowing in the nanowire to transition from the switching current to the retrapping current value with a time constant τ_1 . The junctions capacitance is estimated using the expression $C_J = c_s A_J = 100$ fF, where $c_s = 50$ fF/ μm^2 is the specific capacitance and $A_J = 2\mu\text{m}^2$ is the junctions surface area.